

Modeling gravitational waves from exotic compact objects

Alexandre Toubiana,^{1,2} Stanislav Babak,^{1,3} Enrico Barausse,^{4,5} and Luis Lehner⁶

¹*APC, AstroParticule et Cosmologie, Université de Paris,
CNRS, Astroparticule et Cosmologie, F-75013 Paris, France*

²*Institut d'Astrophysique de Paris, CNRS & Sorbonne Universités, UMR 7095, 98 bis bd Arago, 75014 Paris, France*

³*Moscow Institute of Physics and Technology, Dolgoprudny, Moscow region, Russia*

⁴*SISSA, Via Bonomea 265, 34136 Trieste, Italy and INFN Sezione di Trieste*

⁵*IFPU - Institute for Fundamental Physics of the Universe, Via Beirut 2, 34014 Trieste, Italy*

⁶*Perimeter Institute, 31 Caroline St N, Ontario, Canada*

Exotic compact objects can be difficult to distinguish from black holes in the inspiral phase of the binaries observed by gravitational-wave detectors, but significant differences may be present in the merger and post-merger signal. We introduce a toy model capturing the salient features of binaries of exotic compact objects with compactness below 0.2, which do not collapse promptly following the merger. We use it to assess their detectability with current and future detectors, and whether they can be distinguished from black hole binaries. We find that the Einstein Telescope (LISA) could observe exotic binaries with total mass $O(10^2) M_\odot$ ($10^4 - 10^6 M_\odot$), and potentially distinguish them from black hole binaries, throughout the observable Universe, as compared to $z \lesssim 1$ for Advanced LIGO. Moreover, we show that using standard black hole templates for detection could lead to a loss of up to 60% in the signal-to-noise ratio, greatly reducing our chances of observing these signals. Finally, we estimate that if the loudest events in the O1/O2 catalog released by the LIGO/Virgo collaboration were ECO binaries as the ones considered in this paper, they would have left a post-merger signal detectable with model-agnostic searches, making this hypothesis unlikely.

I. INTRODUCTION

In the standard astrophysical paradigm, the only compact objects (with compactness $C = GM/Rc^2 \gtrsim 0.1$ where M is the mass of the object and R its radius) are black holes (BHs) and neutron stars (NSs). Among these, BHs are the only ones that can have mass above $3 M_\odot$. Within this paradigm, extensive efforts have provided theoretical guidance for the search, detection and analysis of gravitational waves (GWs) from binary black holes (BBHs), binary neutron stars (BNSs) and neutron star–black hole binaries. To date, detections by the LIGO/Virgo collaboration (LVC) [1, 2] are in solid agreement with these predictions [3–10]. Nevertheless, the availability of data and its gradually improving accuracy offer compelling motivations for exploring possible extensions of this paradigm. For instance, extensions of General Relativity (GR) and/or of the Standard Model can give rise to “exotic compact objects” (ECOs). Examples of ECOs are boson stars (BSs), see [11] and references therein, gravastars [12, 13], wormholes [14], fuzzballs [15] and firewalls [16]; see also [17–20] for further possibilities and [21] for a review. ECOs can have masses ranging from $O(1M_\odot)$ to $O(10^9 M_\odot)$ and compactnesses ranging from 0.1 to 0.5¹, thus mimicking the gravitational behavior of BHs and NSs to varying degrees. For this reason, their identification is potentially difficult, requiring the use of specific gravitational wave templates to distinguish them. Unfortunately, the vast majority of models of ECOs are not yet complete enough to construct their corresponding gravitational wave templates, especially in the binary merger case, with the exception of (some types of) binary boson stars (BBSs). Furthermore, even for BBSs, full solutions are avail-

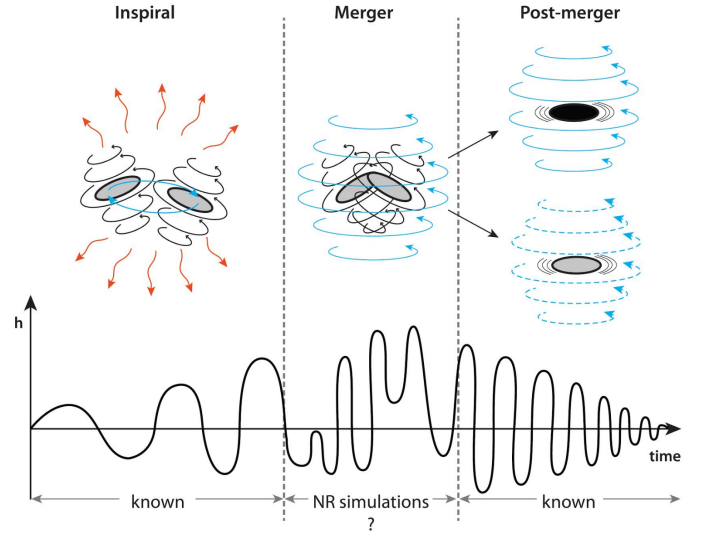


FIG. 1. Schematic representation of our knowledge of the GW signal emitted by an ECO binary: within GR we have a good idea of the qualitative features of the inspiral and post-merger, but the connection between these two regimes is still largely unknown. We expect that the merger leads to the formation of either a BH or an (excited) object of the same nature as the initial ECOs, possibly rotating. The remnant relaxes through emission of GWs, which are related to its fundamental properties and/or the dynamics of the merger.

able only in a small number of cases [22–24]. The lack of templates beyond the standard paradigm could spoil our chances of observing these systems, because the signal to noise ratio (SNR) is highest with matched filtering techniques. In a sense, the current state of knowledge outside the standard BH/NS paradigm, illustrated in Fig. 1, resembles the situation

¹ We recall that the minimum compactness of stationary BHs in GR is 0.5.

in the early 2000s for BBHs within GR². At that epoch, only the early inspiral and post-merger phases had been reasonably modeled, while no numerical-relativity (NR) simulations for the merger phase were available until [26–28] and the large body of work since then.

One expects that for ECO binaries a post-Newtonian (PN) description furnishes a fairly good representation of the binary’s behavior in the early inspiral. GW signals should be well described by the point-particle binary model until tidal effects become apparent. After coalescence, it is natural to expect either an object of the same nature as the initial bodies or a BH. The GWs emitted in this regime would be related to fundamental properties of the corresponding object and/or the dynamics of the merger. However, the details of the coalescence phase, which contains precious information on the properties of the original bodies (see Sec. II), are unknown. For this reason, studies on the possibility of distinguishing ECOs from standard compact objects with GWs have focused mainly on these two regimes, e.g. through perturbative modifications to the inspiral signal [29–41], quasinormal modes (QNM) of ECOs [42–47] or echoes after the merger [48–61]. In order to fully exploit the potential of GW observations and ready the analysis required to discern ECOs through the full inspiral, merger and post-merger phases, we propose a toy model aiming to capture the main features of the full GW signal emitted by ECO binaries.

This paper is organized as follows. In Sec. II we discuss known features of the merger of non-BH compact objects, which we utilize to construct the toy model presented in Sec. III. We describe how the full GW signal is built in Sec. IV. In Sec. V we assess the detectability of ECO binaries and our ability to distinguish them from standard compact binaries with current and future GW detectors. Finally, we present our conclusions in Sec. VI.

II. COALESCENCE OF COMPACT OBJECTS OTHER THAN BLACK HOLES

To construct our model, we will rely on our understanding of BBHs together with BNSs and BBSs. In particular, the differences of the latter two systems with BBHs will inform us how to implement in our model the particular phenomenology that general ECOs might display. For simplicity, we focus on binaries consisting of (nonspinning) identical objects (same nature and same mass) on quasicircular orbits. Here and throughout this paper, we denote by m_0 and r_0 the mass and radius of the bodies, and their compactness in isolation by $C_0 = Gm_0/r_0c^2$.

During the inspiral phase of BNSs and BBSs, tidal effects lead to a correction in the GW phase at 5PN order relative to BBHs [62–64] (in GR). This correction is proportional to the dimensionless tidal polarizability: $\Lambda = \frac{2}{3}k_2C_0^{-5}$ [63, 64], k_2 being the tidal Love number. The compactness and the tidal

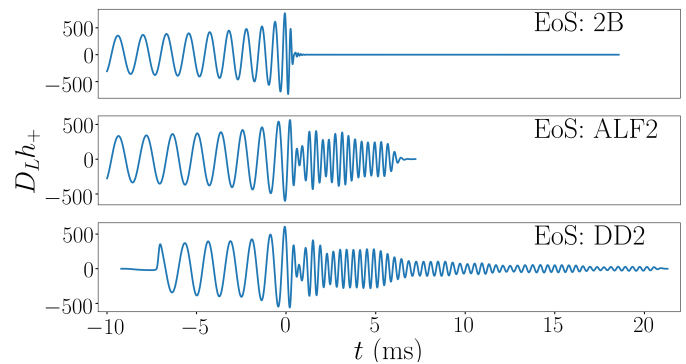


FIG. 2. Numerical simulations of BNS waveforms for different EoSs. For the 2B EoS, the system promptly collapses to a BH after contact. For the ALF2 and the DD2 EoS, a hypermassive NS is formed following contact. In the former case the hypermassive NS ends up collapsing to a BH after $\simeq 7$ ms, whereas in the latter case it does not collapse for the duration of the simulation, seemingly relaxing to a stable NS.

Love number are determined by the equation of state (EoS). NSs typically have C_0 in the range 0.14 – 0.2 (see Fig. 7 of [65]). To date, proposed models for nonspinning BSs give similar values, but can reach higher compactness (so far, up to 0.3 [66, 67]). As for k_2 , it is typically of the order of 0.1 for NSs and currently available models of BSs [29, 31, 68–70].

The PN description fails when the stars come in contact. This approximately takes place at the “contact frequency”

$$f_c = \frac{c^3}{2G} \frac{C_0^{3/2}}{m_0}, \quad (2.1)$$

which depends on the EoS through the compactness. For low enough values of C_0 ($\lesssim 0.29$), this frequency is lower than that of the innermost stable circular orbit for a BBH of the same mass. For this reason, we will employ the terminology “post-contact” rather than merger/post-merger whenever appropriate. For ultracompact exotic objects, $C_0 \sim 0.5$ and the objects reach the innermost stable circular orbit before touching. We thus expect the merger to proceed in a fashion more similar to BBHs, with no post-contact stage. However, no numerical simulations in this regime are available so far to confirm this expectation. Moreover, it is possible that such objects do not exist in nature as they might be nonlinearly unstable [71]. After contact, a rather complex behavior is displayed by BNSs and BBSs (and thus potentially also by ECO binaries), while the system’s evolution is comparatively simpler in the case of BBHs. This behavior is only explorable through numerical simulations.

After the stars touch, the least bound material might be disrupted (and a portion of it might even be ejected), whereas the remaining part gives rise to an envelope containing the inner cores of the original bodies [22, 72]. Gravitational interaction acts to bring the cores together, but internal restoring forces (whose exact nature depends on the objects) and angular momentum oppose it. As a result, collapse to a BH can be prevented, forming instead a hypermassive star [22, 73].

² Fig. 1 is largely inspired from Fig. 9 in [25].

As these effects compete, the cores oscillate [22, 72]. Eventually, collapse to a BH or formation of a stable star ensues. The exact outcome is determined by the total mass of the system, the EoS and any further relevant physics at play (e.g. microphysics, electromagnetic effects and gravitational cooling)[24, 74–76].

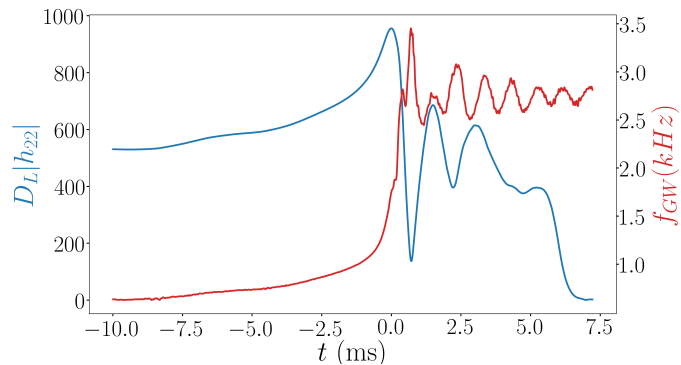


FIG. 3. Amplitude-frequency decomposition of the GW signal emitted by a BNS following the ALF2 EoS. The signal is characterized by the oscillations in amplitude (blue) and frequency (red) in the post-contact stage.

These different scenarios leave distinct imprints on the waveform, as can be seen in Fig. 2. There, we display the GW signal produced by the merger of two NSs with initial masses $m_0 = 1.35 M_\odot$, for different choices of the EoS: 2B [77], ALF2 [77] and DD2 [78]. The merger happens at $t = 0$. The waveforms that we show were taken from the CoRe database³ [79]. The system in the upper panel collapses immediately to a BH following contact, whereas the other two form a hypermassive NS. The system in the middle panel collapses to a BH after ~ 7 ms, and the one in the lower panel does not collapse for the simulation duration, seemingly forming a stable NS. In the last two cases, the difference with a BBH signal is visible with naked eye. Fig. 3 shows the decomposition of the signal obtained with the ALF2 EoS (middle panel of Fig. 2) into amplitude and frequency. We note that the post-contact signal is characterized by oscillations in the GW amplitude and frequency.

Remarkably, for some models of BSs, if the outcome is a BS, angular momentum is entirely radiated immediately after contact, with very little mass ejected [22, 23, 80, 81]. The hypermassive BS radiates GWs primarily at the fundamental quasinormal frequency of the star [22]. On the other hand, for BNSs the main frequencies in the post-contact stage are determined by the dynamics of the binary [82–85].

With these observations in mind, we propose that the coalescence of ECO binaries should consist of (i) an inspiral phase with tidal effects (ii) a post-contact evolution with three possible scenarios:

- prompt collapse to a BH,
- formation of a hypermassive ECO that ultimately collapses to a BH,

- formation of a hypermassive ECO that settles into a stable remnant of the same nature as the original bodies.

Moreover, we expect the amount of angular momentum retained in the post-contact evolution to depend on the nature of the original bodies. We introduce a parameter $0 \leq \kappa \leq 1$ that represents the fraction of angular momentum retained at the onset of the post-contact phase. This parameter depends on the nature of the compact objects, and it is related to the ability of a given compact object to sustain rotation. For instance, it would be ~ 1 (~ 0) in case a stable remnant forms from the coalescence of a BNS (some models of BBS). This generic classification allows for a model agnostic phenomenological description of the coalescence of ECO binaries, irrespective of the exact nature of the involved bodies. In this work, we focus on the last two scenarios, and consider only extremal values of κ : we take $\kappa = 1$ for the scenario where a BH is formed as the result of the collapse of a hypermassive ECO, and $\kappa = 1$ or $\kappa = 0$ for the scenario where a stable remnant is formed. Thus, we consider three types of behavior in the post-contact stage:

- **RBH**: rotating systems that collapse to a BH
- **RS**: rotating systems that form a stable remnant
- **NRS**: non-rotating systems that form a stable remnant

We focus on bodies with compactness in the range $0.14 \lesssim C_0 \lesssim 0.2$, which contains the typical values of many models of stable compact objects other than BHs. For high values of C_0 , the toy model that we present in the next section predicts a prompt collapse to a BH, a scenario on which we do not focus. This is in agreement with the numerical simulations available so far, which suggest that for C_0 higher than ~ 0.18 , the coalescence of BBSs leads to a BH [22–24]. However, one should keep in mind that for EoSs that have not been explored yet, or for different setups, it might be possible to form more compact remnants. In particular, stable BSs can reach compactnesses of ~ 0.3 [66, 67], suggesting such endstates might be viable. (Objects with higher compactness, however, might not be stable [71], in which case they would not be a possible coalescence end product.) Our framework could be modified to account for these cases, e.g. by attaching a rotating bar instead of the toy model presented in this work.

III. TOY MODEL

Our starting point is the toy model introduced in [86] to describe the post-contact dynamics of BNSs. We model the inner cores of the ECOs by point particles interacting gravitationally, but also through an effective spring. The latter mimics the effect of the restoring forces, making the cores bounce. The disrupted material is modeled by a disk containing the two point particles, see Fig. 4. For RBH and RS systems the disk and the cores corotate, for NRS systems neither the disk nor the cores rotate.

The toy model is characterized by four free parameters: the radius of the disk (R), the mass of the cores ($m/2$), the spring

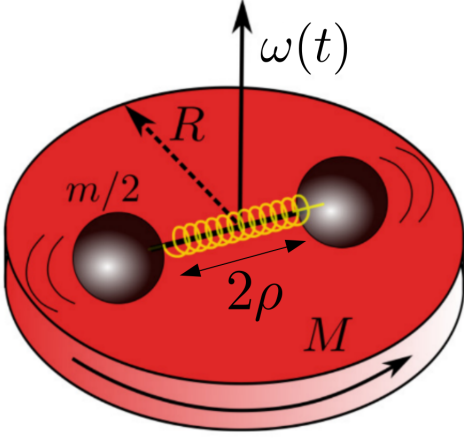


FIG. 4. Illustration of the setup we use to model the dynamics of the post-contact stage, adapted from [86]. The hypermassive ECO is treated as a disk containing two point particles that interact gravitationally, but also through an effective spring. The latter mimics the effect of the restoring forces, making the cores bounce.

constant (k) and its length at rest $2\rho_0$. We assume mass conservation (i.e. no ejection of mass following contact) and that the two point particles have the same mass $m/2$. Therefore, the mass of the disk is $M = 2m_0 - m$, and its radius satisfies $r_0 \leq R \leq 2r_0$. We define the characteristic frequency of the spring as $\omega_0 = \sqrt{k/m}$. These free parameters should be related to the EoS of the ECOs in the binary, e.g. higher values of k correspond to stiffer EoSs (see [87] for a discussion in the case of BNSs). Within this toy model, the three types of post-contact evolution (*RBH*, *RS* and *NRS*) are distinguished by the choice of free parameters and the prescription for the angular momentum.

The dynamics is governed by four variables: the distance of each core to the center (ρ); the orbital angle (ϕ), out of which we define the orbital velocity ($\omega = \dot{\phi}$); the total energy (E); and the total angular momentum (J). Quantities labeled by c refer to the time of first contact, and those labeled by i refer to the beginning of the toy model. We assume that, due to the finite shock-propagation speed, after the two objects touch, only their inner parts are compressed, whereas the outer layers keep their original sizes. We can therefore write $\rho_i = R - r_0$. We assume energy conservation and assume $J_i = \kappa J_c$, where κ is 0 for *NRS* systems and 1 otherwise. The initial orbital phase plays no role in the dynamics, and will be used later to match the post-contact stage to the inspiral.

We map the dynamics to that of an effective particle of mass given by the system's reduced mass, evolving in a potential well $V_{\text{eff}} = V_{\text{centrifugal}} + V_{\text{spring}} + V_{\text{gravitational}}$. The gravitational term was not accounted for in [86], and its expression, together with the centrifugal force and the spring terms, is given in App. A. The addition of the gravitational term allows for a wider variety of post-contact behaviors, and helps provide a natural description of collapse to a BH. Moreover, the treatment of [86] can be seen as a particular case of ours, in the limit of high values of k (stiffer objects), where the spring term dominates over the gravitational one. The shape of the

effective potential is determined by the free parameters of the model. In Fig. 5 we display by dark-red lines the effective potential and the energy (in rescaled dimensionless units) at the start of the post-contact stage, for a given choice of the free parameters (corresponding to an *RS* system). The effective particle is trapped between an inner and an outer turning point, reproducing the oscillatory behavior described in Sec. II. As the system evolves, energy and angular momentum are dissipated through radiation of GWs. Due to the dependence of the centrifugal potential on the angular momentum, the effective potential changes during the evolution, as illustrated by the solid dark-blue line in Fig. 5.

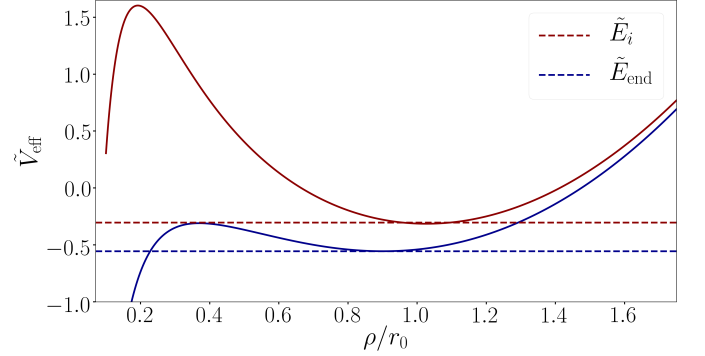


FIG. 5. Evolution of the effective potential and the energy for an *RS* system. As the evolution proceeds, the energy reaches the minimum of the potential, leading to a “circularization” of the orbit.

The evolution of the effective particle is governed by

$$\dot{\phi} = \omega = \frac{J}{I} = \frac{J}{\frac{MR^2}{2} + m\rho^2}, \quad (3.1)$$

$$\dot{\rho} = \pm \sqrt{\frac{2}{m} \sqrt{E - V_{\text{eff}}(\rho)}}, \quad (3.2)$$

$$\dot{E} = -P_{\text{GW}}, \quad (3.3)$$

$$\dot{J} = -J_{\text{GW}}. \quad (3.4)$$

We compute the energy and angular momentum carried away by GWs consistently, using the adiabatic approximation and averaging over an entire period of the radial motion. Details of the computation are given in App. B. We integrate the adiabatic equations of motion, Eqs. (3.1), (3.2), (3.3) and (3.4), over successive periods, see Apps. C and D for details. The evolution proceeds differently for each type of ECO binary:

- For *NRS* systems, one has $J = 0$ and thus the potential is fixed. As the evolution proceeds, the effective particle loses energy and sinks to the bottom of the potential. Physically, this corresponds to the formation of a stable object of the same nature as the binary's ECOs, with zero angular momentum. We fix the parameters of the toy model to match the frequency of the radial oscillations to numerical simulations of BBSs [22] (in principle we could also use QNMs of different ECO models, although numerical simulations are needed in order to check that these are the relevant frequencies in this regime, as was explicitly done in [22].)

- For *RS* systems, the effective particle sinks to the bottom of the potential (see Fig. 5) and the orbit “circularizes”. The system keeps emitting GWs as it settles into an equilibrium state, corresponding to the formation of a stable object of the same nature as the original ECOs.
- For *RBH* systems, the energy eventually becomes larger than the potential height, leading to a “plunge” and subsequent formation of a BH. Following the hoop conjecture [88], we assume that a BH is formed when the compactness of the system becomes larger than 0.5 (the minimum compactness of a BH). The compactness of the system is defined as

$$C_\rho = \frac{GM_\rho}{\rho c^2}, \quad (3.5)$$

where $M_\rho = m + M(\rho/R)^2$ is the total mass within the radius ρ . The BH thus formed has mass $M_f = M_\rho$ and dimensionless spin parameter $a_f = cJ_\rho/GM_\rho^2$, where $J_\rho = (m + M(\rho/R)^2)\rho^2\omega$ is the angular momentum of the collapsing matter out of which the BH forms.

We display examples of the post-contact dynamics of an *RBH* and an *RS* system in App. E. We found the results of this toy model to be more sensitive to the compactness rather than to the exact values of the free parameters. In the remainder of this paper, we present results obtained with choices of the free parameters that we consider to be representative of each type of ECO binary.

IV. WAVEFORM

A. Time domain

We focus on the dominant 22-mode of the GW signal emitted by an ECO binary and match smoothly its amplitude and phase across the different stages of the evolution. We recall that for a GW signal emitted along the direction of the orbital angular momentum, one has $h_{22} = \sqrt{\frac{4\pi}{5}}(h_+ - ih_\times)$. Defining $h_{22} = A(t)e^{-i\Psi(t)}$, the instantaneous GW frequency is given by $\hat{f} = \frac{1}{2\pi} \frac{d\Psi}{dt}$.

1. Inspiral

For the inspiral, we use the effective-one-body waveform SEOBNRv4T, an extension of SEOBNRv4 [89] accounting for tidal effects⁴, and take $k_2 = 0.1$. We stop the inspiral waveform at contact, i.e. when $\hat{f} = 2f_c$. We assume that the formation of the hypermassive star happens over a time interval $\Delta t = 1/2f_c$, which corresponds to half a period after contact. For $m_0 = 1.35 M_\odot$, this gives $\Delta t \simeq 0.7$ ms, in good

agreement with numerical simulations of BNSs. The inspiral is matched to the post-contact waveform over this interval, using cubic functions to ensure smoothness of the amplitude and the instantaneous GW frequency.

2. Post-contact

During this stage the waveform is computed using the quadrupole formula, see App. B. It yields

$$h_+ = \frac{2}{D_L} \frac{G}{c^4} (\gamma_2 \cos(2\phi) - \gamma_1 \sin(2\phi)), \quad (4.1)$$

$$h_\times = \frac{2}{D_L} \frac{G}{c^4} (\gamma_1 \cos(2\phi) + \gamma_2 \sin(2\phi)), \quad (4.2)$$

where

$$\gamma_1 = \frac{2m\rho\dot{\rho}\omega(MR^2 + m\rho^2)}{\frac{MR^2}{2} + m\rho^2}, \quad (4.3)$$

$$\gamma_2 = m \left(\dot{\rho}^2 - \rho^2 \omega^2 - 4\omega_0^2 \rho(\rho - \rho_0) - \frac{Gm}{8\rho} + \frac{GM\rho}{R^2} \right). \quad (4.4)$$

The phase and amplitude of the 22-mode are given by

$$A(t) = \sqrt{\frac{16\pi}{5}} \frac{G}{D_L c^4} \sqrt{\gamma_1^2 + \gamma_2^2}, \quad (4.5)$$

$$\Psi(t) = 2\phi - \arctan(\gamma_1/\gamma_2). \quad (4.6)$$

The initial orbital phase (ϕ_i) is fixed by matching to the inspiral. For *NRS* systems one has $\gamma_1 = 0$ and $\phi = \phi_i$; therefore, with our definition, the instantaneous frequency would vanish in the post-contact phase. In this particular case, we define it instead as the frequency of radial oscillations.

3. Ringdown

For *RBH* systems, we model the ringdown signal of the final BH using the model presented in [91, 92],

$$h_{22}^{\text{RD}}(t) = \eta \tilde{A}_{22}(t) e^{i\tilde{\phi}_{22}(t)} e^{-i\sigma_{220}(t - t_{\text{match}}^{22})}, \quad (4.7)$$

where t_{match}^{22} is the matching time and $\sigma_{220} = -\sigma^I + i\sigma^R$ is the least damped QNM frequency of a perturbed Kerr BH, computed from by [93]. The BH mass and spin are computed as described below Eq. (3.5). The functions $\tilde{A}_{22}(t)$ and $\tilde{\phi}_{22}(t)$ are defined by

$$\tilde{A}_{22}(t) \equiv c_1^c \tanh \left[c_1^f (t - t_{\text{match}}^{22}) + c_2^f \right] + c_2^c, \quad (4.8)$$

and

$$\tilde{\phi}_{22}(t) = \phi_1 - d_1^c \log \left[\frac{1 + d_2^f e^{-d_1^f (t - t_{\text{match}}^{22})}}{1 + d_2^f} \right]. \quad (4.9)$$

Coefficients with superscripts f are calibrated against numerical simulations (the expressions are given in [91, 92]). Those

⁴ This approximant is available in the LIGO Algorithm Library [90].

with superscripts c are used to ensure continuity of the amplitude, phase and their first derivatives at the matching time, while ϕ_1 is the phase at the start of the ringdown. With these matching prescriptions, the phase and the amplitude are C^1 functions.

Our model could also incorporate different behaviors for the final stage, such as resonant modes of excited stars for RS systems, but we do not explore this possibility in this work.

4. Full waveform

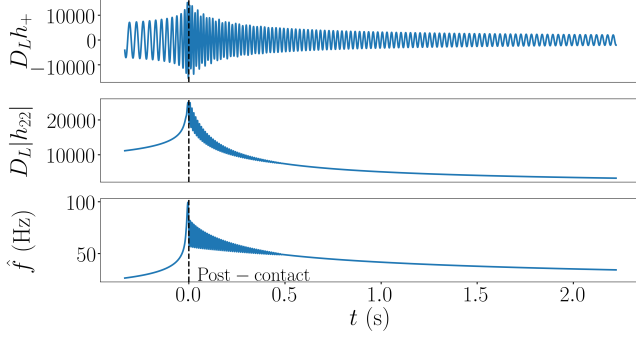


FIG. 6. Waveform for an RS system with $m_0 = 30 M_\odot$ and $C_0 = 0.17$. We show the real part of the 22-mode and its decomposition into amplitude and frequency. The black dashed lines indicate the start of the post-contact stage.

In Figs. 6 and 7 we display the real part of the 22-mode, together with its decomposition in amplitude and frequency for an RS and an RBH system with $m_0 = 30 M_\odot$ and $C_0 = 0.17$. For the sake of clarity, we display only the last instants of the inspiral. The start of the post-contact signal is indicated with black dashed lines. Our model reproduces qualitatively the oscillatory behavior of the GW amplitude and frequency in the post-contact stage. For the RBH system, \hat{f} increases up to the ringdown frequency, whereas for the RS system it tends to zero as the system settles into a stable ECO. For completeness, in Fig. 8 we show the real part of the 22-mode for an NRS system with the same mass and compactness.

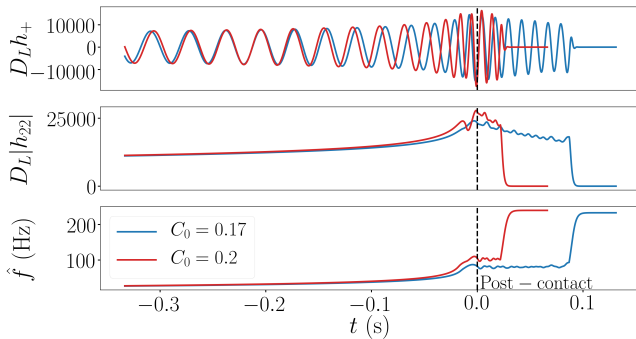


FIG. 7. The same as Fig. 6, but for an RBH system with $m_0 = 30 M_\odot$ and $C_0 = 0.17$ ($C_0 = 0.2$) in blue (red). After contact, the collapse to a BH happens faster for more compact systems.

In Fig. 7 we overplot in red the evolution for a more compact system ($C_0 = 0.2$). This comparison has to be performed carefully: if we were to align the waveforms at the same reference frequency, the signal of the less compact binary would be shorter, because less compact objects touch earlier. Here, we aligned the waveforms at their respective contact frequencies to highlight the post-contact evolution (the apparent alignment ~ 0.25 s before the merger is coincidental). After contact, the collapse to a BH happens faster for more compact objects. Moreover, more compact binaries emit GWs in the post-contact stage at higher frequencies, as expected since their contact frequency is higher.

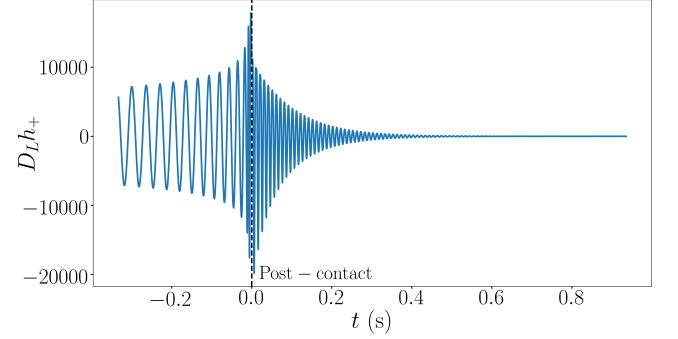
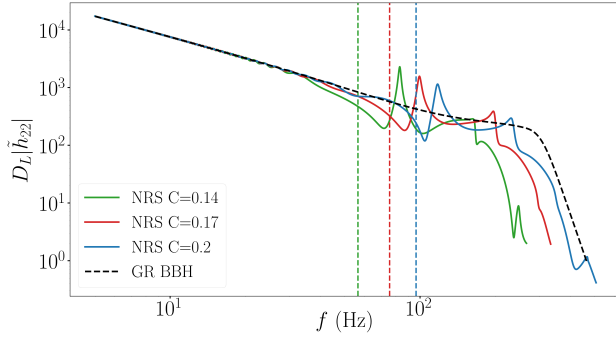


FIG. 8. Real part of the 22-mode for an NRS system with $m_0 = 30 M_\odot$ and $C_0 = 0.17$.

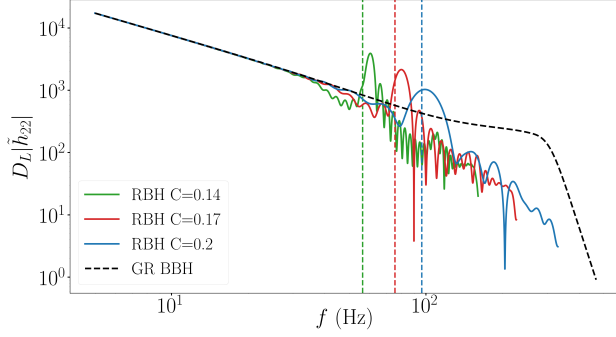
B. Frequency domain

We obtain the frequency domain signal \tilde{h}_{22} by performing a discrete Fourier transform. In Fig. 9 we display the amplitude of \tilde{h}_{22} for the different types of ECO binaries of component masses $30 M_\odot$. Different colors correspond to different C_0 , and the dashed lines indicate the corresponding GW frequency at contact. For comparison, we show the amplitude for a GR BBH with the same component masses and zero spins, obtained with the IMRPhenomD inspiral-merger-ringdown model [94, 95], in black dashed lines. Each type of ECO binary exhibits characteristic features in its signal:

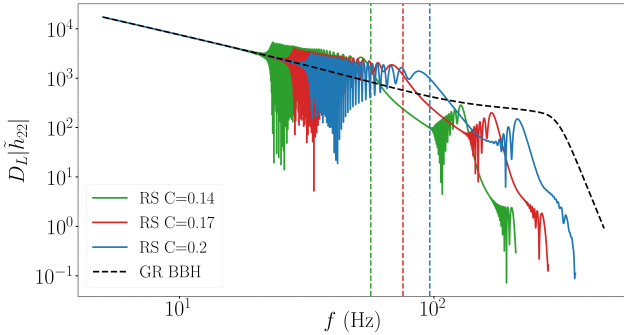
- For NRS systems (upper panel), $|\tilde{h}_{22}|$ presents one main peak at the frequency of radial oscillations, and smaller peaks at the corresponding higher harmonics.
- For RBH systems (middle panel), we observe a main peak at the same frequency around which \hat{f} oscillates in Fig. 7. Beatings between orbital and radial frequencies lead to significant power being emitted at higher and lower frequencies too. As a consequence, the inspiral and post-contact signal “interfere”, leading to wiggles around the transition frequency $2f_c$. The beatings (and therefore the “interference”) and the amplitude of the peak are reduced for more compact configurations, because the post-contact signal is shorter. Moreover, as the compactness increases the signal becomes more and more similar to a BBH signal.



(a) In the post-contact stage, *NRS* systems emit almost exclusively at the frequency of radial oscillations and the corresponding higher harmonics.



(b) For *RBH* systems, we observe a main peak at the frequency around which \hat{f} oscillates in Fig. 7. There is also considerable power emitted at lower and higher frequencies. Thus, the inspiral and post-contact signals “interfere”, leading to wiggles around $2f_c$.



(c) For *RS* systems, \hat{f} tends to zero (see Fig. 6), and the peak observed in *RBH* systems is therefore spread over lower frequencies, leading to significant “interference” with the inspiral signal. The repetition of an oscillatory pattern can be observed at higher frequencies.

FIG. 9. Amplitude of the frequency-domain signal of the three types of ECO binaries, for different values of the initial compactness. The vertical dashed lines indicate the corresponding value of $2f_c$ for each C_0 .

- For *RS* systems (lower panel), \hat{f} tends to zero (see Fig. 6), thus spreading the peak observed for *RBH* systems over lower frequencies. This leads to strong interferences between the inspiral and the post-contact signal, and a highly oscillatory behavior ensues. We identify the repetition of an oscillatory pattern at different frequencies, corresponding to “harmonics” of the sig-

nal.

V. DATA ANALYSIS

We can now assess the detectability of ECO binaries and how well we could distinguish them from BBHs with different GW detectors. We consider ECO binaries with source frame masses in the ranges $[5M_\odot, 10^4 M_\odot]$ and $[10^3 M_\odot, 10^9 M_\odot]$, which could be probed by ground-based detectors and by the Laser Interferometer Space Antenna (LISA) [96], respectively. In the following, it will be convenient to use both *source-frame* (subscript s) and *detector-frame* (subscript d) masses. The two are related by $m_{0,d} = (1+z)m_{0,s}$, where z is the cosmological redshift. We adopt the cosmology inferred by the Planck mission [97]. We start by reviewing a few notions of data analysis and describing the specifics of the detectors.

A. Definitions

The strain measured by ground-based detectors can be written as

$$h = \mathcal{F}_+(\theta, \varphi, \psi, \iota) h_+ + \mathcal{F}_\times(\theta, \varphi, \psi, \iota) h_\times, \quad (5.1)$$

where \mathcal{F}_+ and \mathcal{F}_\times are the extended antenna pattern functions of the detector, including the dependence on the inclination angle (ι) in addition to the declination (θ), right ascension (φ) and polarization (ψ) angles. For a given GW detector, we define the inner product between two templates h_1 and h_2 as [98]

$$(h_1|h_2) = 2 \int_{f_{\min}}^{f_{\max}} \frac{\tilde{h}_1(f) \tilde{h}_2^*(f) + \tilde{h}_1^*(f) \tilde{h}_2(f)}{S_n(f)} df, \quad (5.2)$$

where $S_n(f)$ is the power spectral density (PSD) of the detector, and the integration limits f_{\min} and f_{\max} depend on the detector and the signal. The overlap is defined as

$$O(h_1, h_2) = \frac{(h_1|h_2)}{\sqrt{(h_1|h_1)(h_2|h_2)}}. \quad (5.3)$$

and the SNR as

$$\text{SNR} = \sqrt{(h|h)}. \quad (5.4)$$

We define the averaged SNR over θ, ϕ, ψ and ι as

$$\langle \text{SNR}^2 \rangle = \int_{f_{\min}}^{f_{\max}} \frac{(\langle \mathcal{F}_+^2 \rangle + \langle \mathcal{F}_\times^2 \rangle) |\tilde{h}_{+, \times}(f)|^2}{S_n(f)} df, \quad (5.5)$$

where $\langle \rangle$ denotes averaging over the angles. Defining n as the number of independent detectors and α as the angle between the arms of a given detector, we have

$$\langle \mathcal{F}_+^2 \rangle = \frac{7}{75} n \sin^2(\alpha), \quad (5.6)$$

$$\langle \mathcal{F}_\times^2 \rangle = \frac{1}{15} n \sin^2(\alpha). \quad (5.7)$$

There is no contribution from polarization mixing because $\langle \mathcal{F}_+ \mathcal{F}_\times \rangle = 0$.

B. Detectors

We consider three ground-based detectors: LIGO Livingston at the time of *GW170817* [99], advanced LIGO (aLIGO) at its design sensitivity [1] and the Einstein telescope (ET) [100–102]. We take respectively $f_{\min} = 23, 10, 5$ Hz and $f_{\max} = 2000, 3000, 8000$ Hz for the integration limits. LIGO Livingston and aLIGO are single detectors with angle between the arms $\alpha = \pi/2$, while ET is made of three detectors with $\alpha = \pi/3$.

For LISA, the expression given in Eq. (5.1) is valid only in the long-wavelength approximation [103], to which we will stick. LISA can then be seen as consisting of two independent detectors with $\alpha = \pi/3$. For more details on the calculation of angle-averaged SNRs in LISA, see [104]. We assume a mission duration of 4 years and adopt the frequency range $f_{\min} = \max(10^{-5} \text{ Hz}, f_{-4\text{yrs}})$ and $f_{\max} = 0.1$ Hz, where $f_{-4\text{yrs}}$ is the frequency of a BBH of same component masses 4 years before merger. This is an optimistic choice, as it allows for observing the inspiral during the whole mission duration, as well as the merger if it happens in band.

C. Detectability and distinguishability

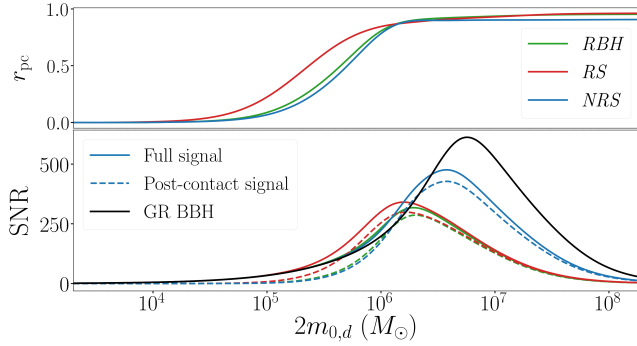
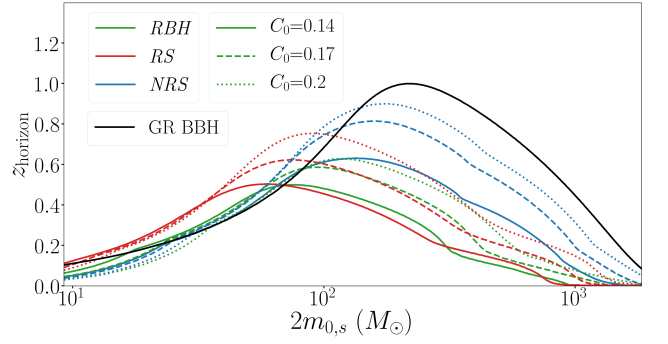


FIG. 10. Lower panel: total and post-contact SNR in LISA as a function of the detector-frame mass, for the three types of ECO binaries. Lower panel: ratio of post-contact to total SNR. We take $C_0 = 0.17$ and place the sources at $z = 10$. As the total mass increases, LISA becomes more sensitive to the post-contact stage and less sensitive to the inspiral, and thence r_{pc} approaches unity.

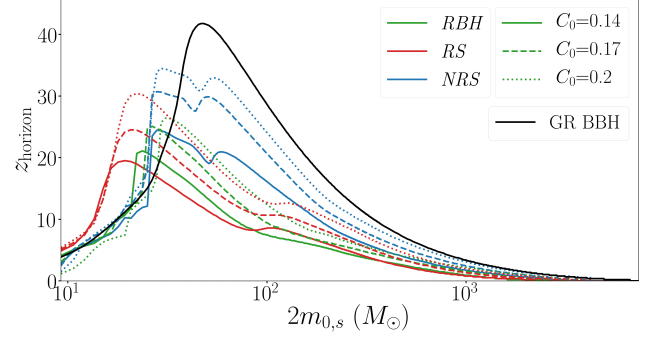
We start by assessing the fraction of SNR coming from the post-contact signal. We define it as

$$r_{\text{pc}} = \sqrt{\frac{\langle \tilde{h}_{\text{pc}} | \tilde{h}_{\text{pc}} \rangle}{\langle \tilde{h}_{\text{tot}} | \tilde{h}_{\text{tot}} \rangle}} = \frac{\text{SNR}_{\text{pc}}}{\text{SNR}_{\text{tot}}}, \quad (5.8)$$

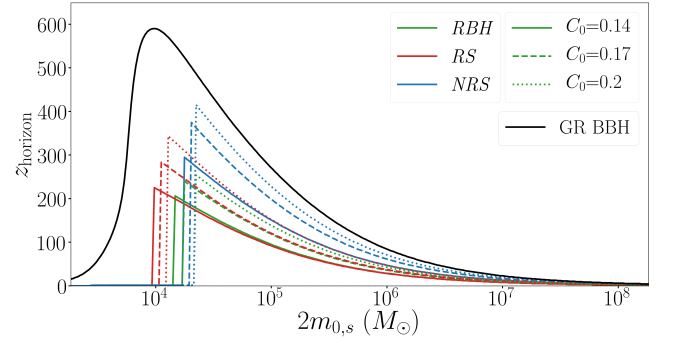
where \tilde{h}_{tot} is the Fourier transform of the whole signal, and \tilde{h}_{pc} is that of the post-contact signal only. In the lower panel of Fig. 10, we display the total (full line) and post-contact (dashed line) SNR in LISA, for the three types of ECO binaries and as a function of the total mass in the detector frame. For comparison, in black we plot the SNR for a binary of non-spinning GR BHs, computed with IMRPhenomD. We place



(a) aLIGO could detect ECO binaries up to $z \approx 1$.



(b) ET could detect ECO binaries with total mass $\mathcal{O}(10^2) M_\odot$ throughout the observable Universe. The double-peaked feature for the NRS system is due to the presence of two lines in the PSD, which damp the contribution of the secondary peak of the frequency-domain signal for masses in between the two maxima.



(c) LISA could detect ECO binaries with total mass $10^4 - 10^6 M_\odot$ throughout the observable Universe. The abrupt cut is due to systems that merge outside the LISA frequency band, but which accrue a large SNR during their inspiral.

FIG. 11. Maximum redshift up to which we could observe and potentially distinguish different types of ECO binaries from BBHs, as a function of the total mass in the source frame. The threshold for observation and distinguishability is set at a total SNR of 8 and at a post-contact SNR of 4, respectively. The maximum redshift typically increases with C_0 and, among ECO binaries, is largest for NRS systems.

the sources at $z = 10$. In the upper panel we plot r_{pc} , which is independent of the redshift. As the total mass increases, LISA becomes more sensitive to the post-contact stage and less to the inspiral, thus r_{pc} approaches unity. The differ-

ence between the various types of systems can be understood from Fig. 9. The post-contact evolution of *RS* systems starts early (at lower frequencies), and the maximum of the SNR is shifted to lower masses than for the other systems. *NRS* systems can reach higher SNRs, because the amplitude of their frequency-domain signal is almost as high as for GR BBHs up to $\approx 2f_c$, thus more SNR is accumulated in this frequency range as compared to *RS* and *RBH* systems, and significant power is emitted at the harmonics of the radial oscillation frequency (more than by BBHs at the same frequency). For lower masses, the total SNR of ECO binaries can even be larger than for BBHs, but it is smaller for higher masses because of the lower emitted power at high frequencies. The picture is similar for ECO binaries in the range $[5M_\odot, 10^4 M_\odot]$ in ground-based detectors.

To gauge our ability to identify these signals, i.e. to detect them and potentially distinguish them from BBHs, we define two thresholds: one for the whole signal and another one for the post-contact signal. Based on studies of the detectability of post-merger signals from BNS coalescence [105–107], we require a minimum SNR for the post-contact signal of 4. Whereas for the overall detectability, we assume a threshold of 8. We define the horizon redshift for the identification of ECO binaries as the maximum redshift such that both thresholds are exceeded. We expect that if both thresholds are exceeded, we should be able to spot the presence of an ECO binary’s post-contact signal in the residuals left after subtracting the best fit GR BBH template from data, and since it is very different from the post-merger signal of BBHs, we should be able to identify the merging objects as being ECOs. Fig. 11 shows the horizon redshift for ECO binaries, as a function of the total mass in the source frame. The upper panel shows results for aLIGO, the middle one for ET and the lower for LISA. For comparison, we plot in black the horizon redshift for a binary of nonspinning GR BHs, computed with IMRPhenomD. The abrupt cut for LISA is due to systems that accumulate a large SNR during their inspiral, but which merge outside the LISA frequency band. Because they can reach higher SNRs, *NRS* systems have the largest horizon among ECO binaries. The horizon distance typically increases with C_0 , because the inspiral of more compact binaries lasts longer, allowing for the accumulation of more SNR. Our results show that aLIGO could identify ECO binaries only up to $z \approx 1$, whereas ET and LISA could identify binaries with total mass $O(10^2) M_\odot$ and $10^4 - 10^6 M_\odot$ respectively, throughout the observable Universe.

Next, we investigate whether the detection of an ECO binary may be mistaken for a BBH. For a given ECO binary signal, we define its fitting factor (FF) [109] as the maximum overlap over GR BBH templates. The FF measures the *effectualness* [110] of a family of templates at reproducing a fiducial signal. The difference $1 - \text{FF}$ yields the SNR fraction that would be lost as a result of the mismatch between the signal and the (best) template. For comparison, template banks are built so that the overlap between neighboring templates is no less than 0.97 [111, 112]. For simplicity, we neglect the dependence on the inclination, declination, right ascension and polarization angles and work with the dominant 22-

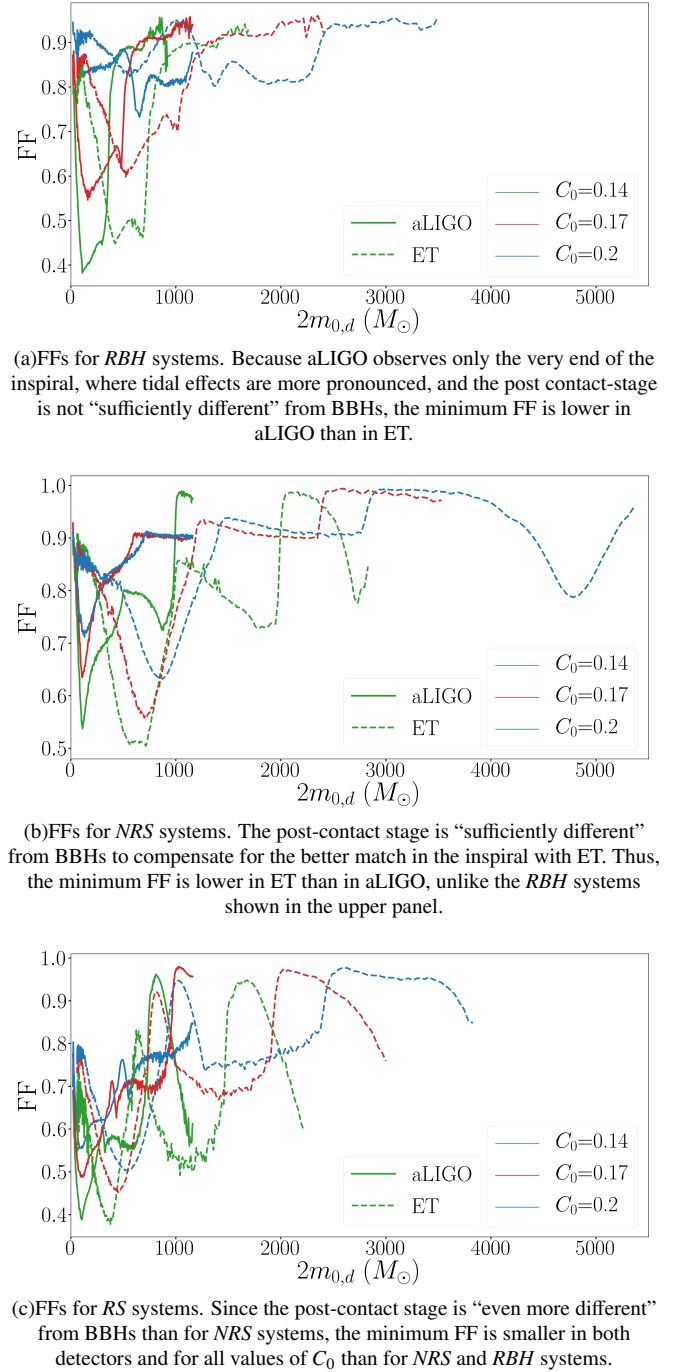


FIG. 12. FF as a function of the total mass in the detector frame, for the different types of ECO binaries (one on each panel) and different values of C_0 (distinguished by the color) in aLIGO (full lines) and ET (dashed lines). Up to 60% of the SNR could be lost if ECO binaries are detected with BBH templates, potentially jeopardizing detection of weaker signals.

mode. Moreover, we restrict ourselves to aligned (or anti-aligned) spins, and maximize over the merger time and the phase at merger as in [113]. Thus, we are left with four parameters over which to maximize: the masses and the spins. For this last step, we use Multinest [114] to search for the

Event	$\mathcal{M}_{c,s} (M_{\odot})$	$m_{0,s} (M_{\odot})$	SNR_{obs}	$C_0 = 0.14$			$C_0 = 0.17$			$C_0 = 0.2$		
				<i>RBH</i>	<i>RS</i>	<i>NRS</i>	<i>RBH</i>	<i>RS</i>	<i>NRS</i>	<i>RBH</i>	<i>RS</i>	<i>NRS</i>
<i>GW150914</i>	28.6	33	24.4	22.1	21.7	21.9	20.5	21.1	20.2	17.1	20.1	18.2
<i>GW150112</i>	15.2	17	10.0	8.0	8.3	7.2	6.9	8.0	6.5	5.2	7.5	5.6
<i>GW151226</i>	8.9	10	13.1	7.4	9.4	6.0	5.9	8.6	5.2	4.0	7.8	4.3
<i>GW170104</i>	21.4	25	13.0	11.2	11.3	11.0	10.3	11.0	10.1	8.3	10.4	8.9
<i>GW170608</i>	7.9	9	14.9	7.6	10.1	6.0	5.9	9.2	5.1	4.0	8.3	4.2
<i>GW170729</i>	35.4	41	10.8	10.3	10.4	10.4	10.0	9.8	9.9	8.8	9.3	9.1
<i>GW170809</i>	24.9	29	12.4	11.1	11.0	11.0	10.3	10.6	10.2	8.5	10.2	9.1
<i>GW170814</i>	24.1	28	15.9	13.7	14.0	13.7	12.8	13.4	12.6	10.4	12.8	11.1
<i>GW170818</i>	26.5	30	11.3	10.3	10.1	10.2	9.6	9.8	9.4	8.0	9.3	8.5
<i>GW170823</i>	29.2	33	11.5	10.8	10.4	10.8	10.2	10.2	10.1	8.7	9.7	9.2

TABLE I. SNR of the post-contact signal for the LVC events, under the hypothesis that those were produced by ECO binaries. We assume equal masses and use the chirp mass and redshift reported in [108] to compute the masses of the binaries components; we also fix the total SNR to the network SNR reported by the LVC (SNR_{obs}).

highest FFs. We compute BBH templates with the IMRPhenomD model.

Fig. 12 shows FFs computed for each type of ECO binary. We use full (dashed) lines for aLIGO (ET). The key information on this figure is given by the range of FFs and the masses for which the FF is minimum. We find that up to 60% of the SNR could be lost if only BBH templates were used in template-based searches, drastically decreasing our chances of detecting these exotic signals. The FF closely resembles inverted SNR (or equivalently the horizon redshift) as a function of the total mass (see Fig. 11), and is minimum for masses that maximize the post-contact SNR. This is why the minimum FF for ET is displaced with respect to aLIGO. The oscillations at higher masses are due to the most salient parts of these exotic signals lying within the most sensitive frequency window of the detector. *RS* and *NRS* systems have lower FFs in ET, whereas for *RBH* systems the minimum FF is lower in aLIGO. This might seem counterintuitive, but it can be understood as follows: (i) aLIGO observes only the very end of the inspiral, where tidal effects are more pronounced and dephasing with BBH templates grows fast; (ii) the post-contact signal of *RS* and *NRS* systems is “sufficiently different” from BBHs, unlike that of *RBH* systems; (iii) the noise level in ET is approximately flat over a broad frequency band, thus ET is more sensitive to the post-contact stage. Similarly, the FF is overall smaller for *RS* systems and higher for *RBH* systems (in agreement with the visual impression from Fig. 9). Finally, the FF increases with C_0 , because ECOs become more similar to BHs as their compactness increases. Since the *effectualness* is always larger than the *faithfulness* [110], our results suggest that the estimation of the parameters of these exotic sources (including masses, spins, etc) could be significantly biased if only GR BBH templates are used.

Finally, we investigate the possibility that the detected BBH events in the first GW catalog released by the LVC [108] may actually be ECO binaries. Because the chirp mass is one of the best constrained parameters, we make the assumption that its measurement is not significantly biased, and use the values reported by the LVC. Moreover, for each event we assume equal masses (all events in the catalog are compatible with this assumption). We estimate the SNR of the post-contact signal by fixing the total SNR to the value measured by the LIGO/Virgo

network, and by using the sensitivity of LIGO Livingston at the time of *GW170817*. Let us stress that the noise level was not the same for all the events, and in particular, the PSD at the time of *GW170817* corresponds to the highest sensitivity reached during the first two observing runs of the LVC. Therefore, our estimates serve as higher bounds on what the real post-contact SNR would have been. The values are reported in Table I. The post-contact SNR decreases with C_0 , because the SNR accumulated during the inspiral is larger for more compact binaries and we have fixed the total SNR. Based on studies of the detectability of the post-contact signal of BNSs [106], our results suggest that the post-contact SNR would be sufficient for detection with wavelet-based pipelines, at least for the loudest sources. The compatibility of the residuals left after subtracting the best fit GR BBH template from data with Gaussian noise [5] makes it unlikely that these events were generated by ECO binaries as the ones considered in this paper (i.e. made of identical objects with $C_0 \leq 0.2$ and which do not collapse promptly following contact).

VI. DISCUSSION

In the next few years, the sensitivity of ground-based GW detectors will improve significantly, increasing the detection rate and our ability to extract the source parameters. Moreover, LISA will allow one to observe a yet unexplored population of massive compact binaries with very high SNR (see e.g. [115–121]). Together, ground-based and space-based detectors will offer us the opportunity to probe the nature of compact objects with exquisite precision. To enhance our chances of detecting exotic signals and properly extracting physical information from the data, we have proposed a simple model that captures the main features of the full GW signal from binaries consisting of identical ECOs with compactness below 0.2 and which do not collapse promptly following contact. We have focused on the BNS and BBS examples to build our model, since these are the only non-BH binary systems for which numerical simulations are available. Nevertheless, the physics that enters the phenomenological description that we propose is sufficiently generic that we expect it to encompass a wide variety of ECO binaries.

We adopt an agnostic approach and distinguish three types of ECO binaries, according to their post-contact evolution. We model the post-contact dynamics with a toy model inspired by knowledge of the coalescence phase of compact objects other than BHs. We then extract the GW signal emitted during the post-contact evolution and match it to the inspiral. In the case of collapse to a BH, we also attach a ringdown signal. Our model can qualitatively reproduce the main features of non-BBH signals observed in numerical simulations.

We have investigated the possibility of detecting these objects and discriminating them from BHs with current and future GW detectors. We find that ET and LISA will allow one to detect and potentially distinguish exotic binaries from BBHs (with total mass $O(10^2) M_\odot$ and $10^4 - 10^6 M_\odot$ respectively) throughout the observable Universe, as compared to up to $z \lesssim 1$ for aLIGO. On the other hand, we find that up to 60% of the SNR could be lost when using BBH templates to search for these exotic signals, thus affecting our chances of observing them. Finally, we have estimated what the post-contact signal would have been like if the events in the first GW catalog released by the LVC were ECO binaries as the ones considered in this paper. We have found that, for the loudest events, the post-contact signal would have been sufficiently strong to be detected by wavelet-based searches, thus making this hypothesis unlikely. Our analysis could be extended to the second catalog released by the LVC [122], including the noteworthy event *GW190521* [9], which has been suggested to be compatible with a BBS signal [123].

In this work, we have focused on distinguishing ECO binaries from BBHs. However, our framework should also allow one to distinguish them from BNSs. For instance, for similar masses, BBSs emit GWs at lower frequencies than BNSs during the post-contact stage. By measuring the masses from the inspiral signal, this feature could allow one to distinguish ECO binaries from BNSs. Moreover, model selection between classes of ECOs may be feasible with our approach. For instance, ECOs retaining a non-negligible amount of orbital angular momentum at merger could be distinguished from those that do not (e.g. BNSs). On the other hand, more subtle effects would require further enhancing our model.

As a follow-up, one could perform a more refined analysis of the exotic signals that we generated, in order to quantify how well physical information can be extracted from them. To this purpose, one may use, for instance, the methods developed for the analysis of the post-contact signal of BNSs [105–107]. On the modeling side, in this work we have considered the angular momentum to be conserved, or completely radiated right after contact. We have observed that these prescriptions lead to very distinct features in the GW signal. Therefore, it would be interesting to consider prescriptions between these two extremes. Finally, additional modifications due to the absence of tidal heating [30, 37] and a multipole structure different from BBHs [33, 34] may occur in the inspiral of ECO binaries. Accounting for them should increase our chances of discriminating these sources from BBHs [41]. Moreover, one could account for ECOs with negative Love numbers as suggested in [31]. Moreover, we could extend our framework to objects with higher compactness, by considering different

prescriptions for the merger/post-merger stage, e.g. attaching a rotating bar instead of the toy model we used in this work.

We have proposed a model for the coalescence of ECO binaries that could serve to test different data analysis strategies. It could be particularly helpful for the design of algorithms looking for deviations from GR BBHs around the merger. Certainly, the detection of such exotic signals would be an exciting discovery.

ACKNOWLEDGEMENTS

We are grateful to Tallulah Frappier for Fig. 1 and to Kentaro Takami, Luciano Rezzolla and Luca Baiotti for their permission to use Fig. 4. We are indebted to Paolo Pani, Caio Macedo, Frank Ohme, Duncan Brown and Tim Dietrich for fruitful discussions during the preparation of this work and to Abhirup Ghosh and Juan Calderón Bustillo for their constructive comments in the final stages of the elaboration of this manuscript. A.T. is thankful to SISSA and Perimeter Institute for their hospitality. This work has been supported by the European Union’s Horizon 2020 research and innovation program under the Marie Skłodowska-Curie grant agreement No 690904. The authors would also like to acknowledge networking support from the COST Action CA16104. S.B. and A.T. acknowledge support by CNES, in the framework of the LISA mission. E.B. acknowledges financial support provided under the European Union’s H2020 ERC Consolidator Grant “GRavity from Astrophysical to Microscopic Scales” grant agreement no. GRAMS-815673.

Appendix A: Potential

The full gravitational potential, accounting for the interaction between the cores, the one between the cores and the disk and the rest energy of the disk is given by

$$V_{\text{gravitational}} = -\frac{Gm^2}{8\rho} - \frac{GmM\rho}{R^2} - \frac{2GM^2}{3R}. \quad (\text{A1})$$

The centrifugal and spring terms are given by

$$V_{\text{centrifugal}} = \frac{1}{2}I\omega^2 = \frac{1}{2} \frac{J^2}{\frac{MR^2}{2} + m\rho^2}, \quad (\text{A2})$$

$$V_{\text{spring}} = 2k(\rho - \rho_0)^2. \quad (\text{A3})$$

Appendix B: Gravitational waves feedback

The conservative equations of motions (for $P_{\text{GW}} = \dot{J}_{\text{GW}} = 0$) are obtained by taking the derivatives of (3.2) and (3.1) and making use of (3.3) and (3.4). They read

$$\ddot{\rho} = \rho\omega^2 - 4\omega_0^2(\rho - \rho_0) - \frac{Gm^2}{8\rho^2} + \frac{GM}{R^2}, \quad (\text{B1})$$

$$\dot{\omega} = -\frac{2m\rho\dot{\rho}\omega}{\frac{MR^2}{2} + m\rho^2}. \quad (\text{B2})$$

The quadrupole momentum of the system is given by

$$M_{ij} = \frac{m\rho^2}{2} \begin{pmatrix} \cos(2\phi) & \sin(2\phi) & 0 \\ \sin(2\phi) & -\cos(2\phi) & 0 \\ 0 & 0 & 0 \end{pmatrix} + \frac{m\rho^2}{6} \begin{pmatrix} 1 & 0 & 0 \\ 0 & 1 & 0 \\ 0 & 0 & -2 \end{pmatrix}. \quad (\text{B3})$$

We call Q_{ij} the transverse traceless part of M_{ij} . Making use of the conservative equations of motion, Eqs. (B1) and (B2), we compute the two polarizations

$$h_+ = \frac{\ddot{Q}_{11} - \ddot{Q}_{22}}{D_L} = \frac{2}{D_L} \frac{G}{c^4} (\gamma_2 \cos(2\phi) - \gamma_1 \sin(2\phi)), \quad (\text{B4})$$

$$h_\times = \frac{2\ddot{Q}_{12}}{D_L} = \frac{2}{D_L} \frac{G}{c^4} (\gamma_1 \cos(2\phi) + \gamma_2 \sin(2\phi)), \quad (\text{B5})$$

where γ_1 and γ_2 have been defined in Eqs. (4.3) and (4.4). The instantaneous power and angular momentum are given by

$$P_{\text{GW}} = \frac{G}{5c^5} \ddot{Q}_{ij} \ddot{Q}_{ij}, \quad (\text{B6})$$

$$J_{\text{GW}} = \frac{2G}{5c^5} \epsilon^{3kl} \ddot{Q}_{ka} \ddot{Q}_{la}. \quad (\text{B7})$$

Using the conservative equations of motion and defining

$$g_2 = \dot{\gamma}_1 + 2\omega\gamma_2$$

$$= -m\dot{\rho} \left(\frac{4MR^2\omega^2\rho}{\frac{MR^2}{2} + m\rho^2} + 4\omega_0^2(4\rho - 3\rho_0) + \frac{Gm}{8\rho^2} - \frac{3GM}{R^2} \right), \quad (\text{B8})$$

$$g_1 = \dot{\gamma}_2 - 2\omega\gamma_1$$

$$= \frac{2m}{\frac{MR^2}{2} + m\rho^2} \left[-\frac{m\rho^2\dot{\rho}^2\omega(3MR^2 + 2m\rho^2)}{\frac{MR^2}{2} + m\rho^2} + \omega \left(\left(\dot{\rho}^2 - 4\omega_0^2(\rho - \rho_0)\rho + \frac{GM\rho}{R^2} - \frac{Gm}{8\rho} \right) \left(\frac{3MR^2}{2} + 2m\rho^2 \right) + \rho^2\omega^2 \frac{MR^2}{2} \right) \right], \quad (\text{B9})$$

we get

$$P_{\text{GW}} = \frac{2}{5} \frac{G}{c^5} (g_1^2 + g_2^2), \quad (\text{B10})$$

$$J_{\text{GW}} = \frac{4}{5} \frac{G}{c^5} (\gamma_2 g_1 - \gamma_1 g_2). \quad (\text{B11})$$

The averaged energy and angular momentum loss are recomputed at the beginning of each cycle.

Appendix C: Quasi-eccentric orbit

Inspired by the equations for eccentric motion, we introduce the phase angle χ such that

$$\rho = \frac{p}{1 + e \cos(\chi)}. \quad (\text{C1})$$

The parameter p and the ‘eccentricity’ e of the orbit can be computed from the turning points ρ_+ and ρ_-

$$p = 2 \frac{\rho_+ \rho_-}{\rho_+ + \rho_-} \quad (\text{C2})$$

$$e = \frac{\rho_+ - \rho_-}{\rho_+ + \rho_-}. \quad (\text{C3})$$

Assuming the adiabatic approximation for e and p holds i.e.

$$\frac{\dot{e}}{e} \ll \frac{1}{T}, \quad (\text{C4})$$

$$\frac{\dot{p}}{p} \ll \frac{1}{T}, \quad (\text{C5})$$

the derivative of Eq. (C1) gives

$$\dot{\rho} = \frac{pe \sin(\chi) \dot{\chi}}{(1 + e \cos(\chi))^2}. \quad (\text{C6})$$

The change of sign in $\dot{\rho}$ is accounted for by $\sin(\chi)$ and the evolution of χ is monotonic. The sign of $\dot{\chi}$ is determined by the initial conditions. For instance, if $\chi_i > 0$, Eq. (3.2) becomes

$$\dot{\chi} = \frac{(1 + e \cos(\chi))^2}{pe |\sin \chi|} \sqrt{\frac{2}{m}} \sqrt{E - V_{\text{eff}}(\rho)}. \quad (\text{C7})$$

The term under the rightmost square root can be written

$$E - V_{\text{eff}} = \frac{-2km(\rho - \rho_+)(\rho - \rho_-)(\rho - \rho_3)(\rho - \rho_4)(\rho - \rho_5)}{\rho(\frac{MR^2}{2} + m\rho^2)}, \quad (\text{C8})$$

where ρ_3 , ρ_4 and ρ_5 are the remaining (possibly complex) roots of $E - V_{\text{eff}} = 0$. Noticing that

$$\rho - \rho_+ = \frac{-pe(1 + \cos(\chi))}{(1 - e)(1 + e \cos(\chi))},$$

$$\rho - \rho_- = \frac{pe(1 - \cos(\chi))}{(1 - e)(1 + e \cos(\chi))},$$

the equation for χ can be recast as

$$\dot{\chi} = \frac{2\omega_0(1 + e \cos(\chi))}{\sqrt{1 - e^2}} \sqrt{\frac{(\rho - \rho_3)(\rho - \rho_4)(\rho - \rho_5)}{\rho(\frac{MR^2}{2m} + \rho^2)}}. \quad (\text{C9})$$

Thus, we evolve numerically Eqs. (C1) and (C9) rather than Eq. (3.2).

For *RBH* systems, when the energy becomes larger than the effective potential height, the inner turning point ceases to exist so we cannot use Eq. (C1) anymore and we turn back to Eq. (3.2) to describe the final moments of the evolution before the collapse to a BH.

Appendix D: Quasi-circular orbit

As the orbit ‘circularizes’, e becomes very small and the adiabatic approximation [Eq. (C4)] ceases to be valid. This happens when the particle reaches the bottom of the potential

well: $V'_{\text{eff}}(\rho) = 0$. This condition allows us to express ω as a function of ρ and we get the new conservative equations of motion

$$\dot{\rho} = 0, \quad (\text{D1})$$

$$\omega^2 = \frac{1}{\rho} \left(4\omega_0^2(\rho - \rho_0) + \frac{Gm}{8\rho^2} - \frac{GM}{R^2} \right). \quad (\text{D2})$$

These expressions are used in Eqs. (B11) and (B11) to write P_{GW} and \dot{J}_{GW} as functions of ρ only. Accounting for the dissipation of energy and angular momentum, the equation for ρ is given by

$$\dot{\rho} = \frac{\dot{E}}{\frac{\partial E}{\partial \rho}} = \frac{\dot{J}}{\frac{\partial J}{\partial \rho}}. \quad (\text{D3})$$

As a sanity check, we verified that the expressions using the angular momentum and the one using the energy give the same equation. Finally, the equations of motion become

$$\begin{aligned} \dot{\rho} = & -\frac{32G}{5c^5} m^2 \omega^2 \rho^2 \left(4\omega_0^2 \rho^2 (\rho - \rho_0) + \frac{Gm}{8} - \frac{GM\rho^2}{R^2} \right)^2 \\ & \times \left[2m\omega_0^2 \rho^2 \left(4(\rho - \rho_0)\rho^2 + \rho_0 \left(\rho^2 + \frac{MR^2}{2m} \right) \right) \right. \\ & \left. + \frac{GM}{2R^2 \rho^2} \left(\frac{MR^2}{2} - 3m\rho^2 \right) - \frac{Gm}{16} \left(\frac{3MR^2}{2} - m\rho^2 \right) \right]^{-1}, \quad (\text{D4}) \end{aligned}$$

$$\omega = \sqrt{\frac{1}{\rho} \left(4\omega_0^2(\rho - \rho_0) + \frac{Gm}{8\rho^2} - \frac{GM}{R^2} \right)}, \quad (\text{D5})$$

$$\begin{aligned} E = & 2m\omega_0^2 \left(\left(\frac{MR^2}{2m} + \rho^2 \right) \left(1 - \frac{\rho_0}{\rho} \right) + (\rho - \rho_0)^2 \right) \\ & + \frac{Gm}{16\rho^3} \left(\frac{MR^2}{2} + m\rho^2 \right) - \frac{GM}{2R^2 \rho} \left(\frac{MR^2}{2} + 3m\rho^2 \right) - \frac{2}{3} \frac{GM^2}{R}, \quad (\text{D6}) \end{aligned}$$

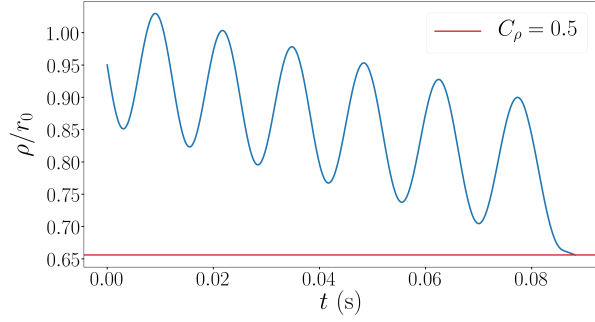
$$J = \left(\frac{MR^2}{2} + m\rho^2 \right) \omega. \quad (\text{D7})$$

Note that taking the $M, k \rightarrow 0$ limit we recover the equations for a quasicircular binary at separation 2ρ . In this regime, ρ tends an equilibrium value corresponding to one of the roots of Eq. (D2), and ω goes to 0. To ensure numerical stability, we switch to this description when $e < 10^{-5}$.

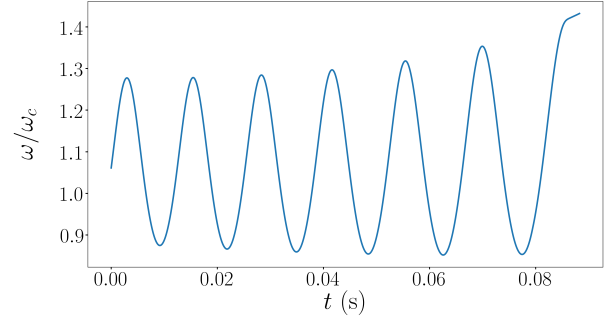
Appendix E: Post-contact dynamics

Fig. 13 shows the post-contact evolution of an *RBH* (upper panel) and an *RS* (lower panel) system with $m_0 = 30 M_\odot$ and $C_0 = 0.17$. In the left panel we display the distance of the cores to the center of mass, which is half the separation between the cores, and in the right panel, the orbital angular velocity. Red solid lines indicate the threshold value of ρ below which a BH is formed, i.e. such that C_ρ , defined in Eq. (3.5), is 0.5. For the *RBH* system, ρ oscillates around a decreasing mean value and, eventually, reaches the threshold value, leading to the formation of a BH. ω oscillates around a stable mean

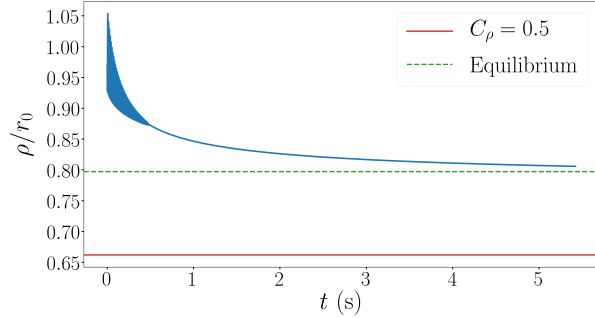
value and increases right before the formation of the BH. This is related to the increase in the GW frequency before the ring-down stage in Fig. 7. For the system we show, the final BH has total mass $M_f = 58 M_\odot$ and dimensionless spin $a_f = 0.39$. In the case of the *RS* system, ρ and ω initially oscillate around a decreasing mean value. The orbit then “circularizes”, from which point both decrease, while the system tends to an equilibrium configuration. The equilibrium value of ρ , indicated by the green dashed line, is higher than the threshold value for collapse. Therefore, a stable ECO is formed. The equilibrium value of ω is 0, this cannot be seen from Fig. 13 because we do not display the long-term evolution for sake of clarity. The evolution of ρ for *NRS* systems is similar to the one of the *RS* system.



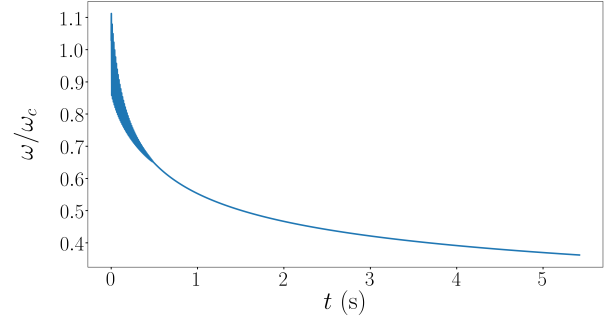
(a) The distance to the center of mass oscillates around a decreasing mean value, until it reaches a value such that $C_\rho = 0.5$, leading to the formation of a BH.



(b) The orbital angular velocity oscillates around a stable mean value and increases right before the formation of the BH.



(c) Initially, the distance to the center of mass oscillates around a decreasing mean value. Once the orbit “circularizes”, ρ decreases while tending to an equilibrium value, corresponding to the formation of a stable ECO.



(d) The orbital angular velocity first oscillates around a decreasing mean value and once the orbit “circularizes”, ω decreases while tending to 0 (not shown in the figure).

FIG. 13. Evolution of the distance of the cores to the center of mass (half the distance between the cores) and the orbital angular velocity for an RBH (upper panel) and an RS (lower panel) system.

-
- [1] J. Aasi et al. Advanced LIGO. *Class. Quant. Grav.*, 32:074001, 2015.
 - [2] F. Acernese et al. Advanced Virgo: a second-generation interferometric gravitational wave detector. *Class. Quant. Grav.*, 32(2):024001, 2015.
 - [3] B.P. Abbott et al. Tests of general relativity with GW150914. *Phys. Rev. Lett.*, 116(22):221101, 2016. [Erratum: *Phys. Rev. Lett.* 121, 129902 (2018)].
 - [4] B.P. Abbott et al. Tests of General Relativity with GW170817. *Phys. Rev. Lett.*, 123(1):011102, 2019.
 - [5] B.P. Abbott et al. Tests of General Relativity with the Binary Black Hole Signals from the LIGO-Virgo Catalog GWTC-1. *Phys. Rev. D*, 100(10):104036, 2019.
 - [6] B.P. Abbott et al. GW190425: Observation of a Compact Binary Coalescence with Total Mass $\sim 3.4M_\odot$. *Astrophys. J. Lett.*, 892(1):L3, 2020.
 - [7] R. Abbott et al. GW190412: Observation of a Binary-Black-Hole Coalescence with Asymmetric Masses. 4 2020.
 - [8] R. Abbott et al. GW190814: Gravitational Waves from the Coalescence of a 23 Solar Mass Black Hole with a 2.6 Solar Mass Compact Object. *Astrophys. J. Lett.*, 896(2):L44, 2020.
 - [9] R. Abbott et al. GW190521: A Binary Black Hole Merger with a Total Mass of $150 M_\odot$. *Phys. Rev. Lett.*, 125:101102, 2020.
 - [10] R. Abbott et al. Tests of General Relativity with Binary Black Holes from the second LIGO-Virgo Gravitational-Wave Transient Catalog. 10 2020.
 - [11] Steven L. Liebling and Carlos Palenzuela. Dynamical Boson Stars. *Living Rev. Rel.*, 20(1):5, 2017.
 - [12] Pawel O. Mazur and Emil Mottola. Gravitational condensate stars: An alternative to black holes. 9 2001.
 - [13] Matt Visser and David L. Wiltshire. Stable gravastars: An Alternative to black holes? *Class. Quant. Grav.*, 21:1135–1152, 2004.
 - [14] Matt Visser. *Lorentzian wormholes: From Einstein to Hawking*. 1995.
 - [15] Kostas Skenderis and Marika Taylor. The fuzzball proposal for black holes. *Phys. Rept.*, 467:117–171, 2008.
 - [16] Ahmed Almheiri, Donald Marolf, Joseph Polchinski, and James Sully. Black Holes: Complementarity or Firewalls? *JHEP*, 02:062, 2013.
 - [17] Mehdi Saravani, Niayesh Afshordi, and Robert B. Mann. Empty black holes, firewalls, and the origin of bekenstein-hawking entropy, 2012.
 - [18] Bob Holdom and Jing Ren. Not quite a black hole. *Physical Review D*, 95(8), Apr 2017.
 - [19] Steven B. Giddings. Possible observational windows for quantum effects from black holes. *Physical Review D*, 90(12), Dec

- 2014.
- [20] Jahed Abedi, Hannah Dykaar, and Niayesh Afshordi. Echoes from the abyss: Tentative evidence for planck-scale structure at black hole horizons. *Physical Review D*, 96(8), Oct 2017.
 - [21] Vitor Cardoso and Paolo Pani. Testing the nature of dark compact objects: a status report. *Living Rev. Rel.*, 22(1):4, 2019.
 - [22] Carlos Palenzuela, Paolo Pani, Miguel Bezares, Vitor Cardoso, Luis Lehner, and Steven Liebling. Gravitational Wave Signatures of Highly Compact Boson Star Binaries. *Phys. Rev.*, D96(10):104058, 2017.
 - [23] Miguel Bezares, Carlos Palenzuela, and Carles Bona. Final fate of compact boson star mergers. *Phys. Rev.*, D95(12):124005, 2017.
 - [24] Miguel Bezares and Carlos Palenzuela. Gravitational Waves from Dark Boson Star binary mergers. *Class. Quant. Grav.*, 35(23):234002, 2018.
 - [25] K.S. Thorne. Space-time warps and the quantum world: Speculations about the future. 2002.
 - [26] Frans Pretorius. Evolution of binary black hole spacetimes. *Phys. Rev. Lett.*, 95:121101, 2005.
 - [27] Manuela Campanelli, C.O. Lousto, P. Marronetti, and Y. Zlochower. Accurate evolutions of orbiting black-hole binaries without excision. *Phys. Rev. Lett.*, 96:111101, 2006.
 - [28] John G. Baker, Joan Centrella, Dae-Il Choi, Michael Koppitz, and James van Meter. Gravitational wave extraction from an inspiraling configuration of merging black holes. *Phys. Rev. Lett.*, 96:111102, 2006.
 - [29] Noah Sennett, Tanja Hinderer, Jan Steinhoff, Alessandra Buonanno, and Serguei Ossokine. Distinguishing boson stars from black holes and neutron stars from tidal interactions in inspiraling binary systems. *Physical Review D*, 96(2), Jul 2017.
 - [30] Andrea Maselli, Paolo Pani, Vitor Cardoso, Tiziano Abdelsalhin, Leonardo Gualtieri, and Valeria Ferrari. Probing Planckian corrections at the horizon scale with LISA binaries. *Phys. Rev. Lett.*, 120(8):081101, 2018.
 - [31] Vitor Cardoso, Edgardo Franzin, Andrea Maselli, Paolo Pani, and Guilherme Raposo. Testing strong-field gravity with tidal Love numbers. *Phys. Rev. D*, 95(8):084014, 2017. [Addendum: *Phys.Rev.D* 95, 089901 (2017)].
 - [32] Gian F. Giudice. Hunting for dark particles with gravitational waves. *EPJ Web Conf.*, 164:02004, 2017.
 - [33] N.V. Krishnendu, K.G. Arun, and Chandra Kant Mishra. Testing the binary black hole nature of a compact binary coalescence. *Phys. Rev. Lett.*, 119(9):091101, 2017.
 - [34] N.V. Krishnendu, Chandra Kant Mishra, and K.G. Arun. Spin-induced deformations and tests of binary black hole nature using third-generation detectors. *Phys. Rev. D*, 99(6):064008, 2019.
 - [35] Nathan K. Johnson-Mcdaniel, Arunava Mukherjee, Rahul Kashyap, Parameswaran Ajith, Walter Del Pozzo, and Salvatore Vitale. Constraining black hole mimickers with gravitational wave observations. 4 2018.
 - [36] Andrea Addazi, Antonino Marciano, and Nicolas Yunes. Can we probe Planckian corrections at the horizon scale with gravitational waves? *Phys. Rev. Lett.*, 122(8):081301, 2019.
 - [37] Sayak Datta, Richard Brito, Sukanta Bose, Paolo Pani, and Scott A. Hughes. Tidal heating as a discriminator for horizons in extreme mass ratio inspirals. *Phys. Rev. D*, 101(4):044004, 2020.
 - [38] Sayak Datta, Khun Sang Phukon, and Sukanta Bose. Recognizing black holes in gravitational-wave observations: Telling apart impostors in mass-gap binaries. 4 2020.
 - [39] Yasmeen Asali, Peter T.H. Pang, Anuradha Samajdar, and Chris Van Den Broeck. Probing resonant excitations in exotic compact objects via gravitational waves. 4 2020.
 - [40] Cecilia Chirenti, Camilo Posada, and Victor Guedes. Where is Love? Tidal deformability in the black hole compactness limit. 5 2020.
 - [41] Costantino Pacilio, Massimo Vaglio, Andrea Maselli, and Paolo Pani. Gravitational-wave detectors as particle-physics laboratories: Constraining scalar interactions with boson-star binaries. 7 2020.
 - [42] Caio F.B. Macedo, Paolo Pani, Vitor Cardoso, and Luís C. B. Crispino. Astrophysical signatures of boson stars: quasinormal modes and inspiral resonances. *Phys. Rev. D*, 88(6):064046, 2013.
 - [43] Vitor Cardoso, Edgardo Franzin, and Paolo Pani. Is the gravitational-wave ringdown a probe of the event horizon? *Phys. Rev. Lett.*, 116(17):171101, 2016. [Erratum: *Phys.Rev.Lett.* 117, 089902 (2016)].
 - [44] Caio F. B. Macedo, Vitor Cardoso, Luís C. B. Crispino, and Paolo Pani. Quasinormal modes of relativistic stars and interacting fields. *Phys. Rev. D*, 93(6):064053, 2016.
 - [45] Nicolas Yunes, Kent Yagi, and Frans Pretorius. Theoretical Physics Implications of the Binary Black-Hole Mergers GW150914 and GW151226. *Phys. Rev. D*, 94(8):084002, 2016.
 - [46] Cecilia Chirenti and Luciano Rezzolla. Did GW150914 produce a rotating gravastar? *Phys. Rev. D*, 94(8):084016, 2016.
 - [47] Elisa Maggio, Luca Buoninfante, Anupam Mazumdar, and Paolo Pani. How does a dark compact object ringdown? 6 2020.
 - [48] Vitor Cardoso, Seth Hopper, Caio F. B. Macedo, Carlos Palenzuela, and Paolo Pani. Gravitational-wave signatures of exotic compact objects and of quantum corrections at the horizon scale. *Phys. Rev. D*, 94(8):084031, 2016.
 - [49] Zachary Mark, Aaron Zimmerman, Song Ming Du, and Yanbei Chen. A recipe for echoes from exotic compact objects. *Phys. Rev. D*, 96(8):084002, 2017.
 - [50] Andrea Maselli, Sebastian H. Völkel, and Kostas D. Kokkotas. Parameter estimation of gravitational wave echoes from exotic compact objects. *Phys. Rev. D*, 96(6):064045, 2017.
 - [51] Randy S. Conklin, Bob Holdom, and Jing Ren. Gravitational wave echoes through new windows. *Phys. Rev. D*, 98(4):044021, 2018.
 - [52] Julian Westerweck, Alex Nielsen, Ofek Fischer-Birnholtz, Miriam Cabero, Collin Capano, Thomas Dent, Badri Krishnan, Grant Meadors, and Alexander H. Nitz. Low significance of evidence for black hole echoes in gravitational wave data. *Phys. Rev. D*, 97(12):124037, 2018.
 - [53] Qingwen Wang and Niayesh Afshordi. Black hole echology: The observer’s manual. *Phys. Rev. D*, 97(12):124044, 2018.
 - [54] Alfredo Urbano and Hardi Veermäe. On gravitational echoes from ultracompact exotic stars. *JCAP*, 04:011, 2019.
 - [55] R.K.L. Lo, T.G.F. Li, and A.J. Weinstein. Template-based Gravitational-Wave Echoes Search Using Bayesian Model Selection. *Phys. Rev. D*, 99(8):084052, 2019.
 - [56] Alex B. Nielsen, Collin D. Capano, Ofek Birnholtz, and Julian Westerweck. Parameter estimation and statistical significance of echoes following black hole signals in the first Advanced LIGO observing run. *Phys. Rev. D*, 99(10):104012, 2019.
 - [57] Ka Wa Tsang, Archisman Ghosh, Anuradha Samajdar, Katerina Chatziioannou, Simone Mastrogiovanni, Michalis Agathos, and Chris Van Den Broeck. A morphology-independent search for gravitational wave echoes in data from the first and second observing runs of Advanced LIGO and Advanced Virgo. *Phys. Rev. D*, 101(6):064012, 2020.

- [58] Elisa Maggio, Adriano Testa, Swetha Bhagwat, and Paolo Pani. Analytical model for gravitational-wave echoes from spinning remnants. *Phys. Rev. D*, 100(6):064056, 2019.
- [59] Baoyi Chen, Yanbei Chen, Yiqiu Ma, Ka-Lok R. Lo, and Ling Sun. Instability of Exotic Compact Objects and Its Implications for Gravitational-Wave Echoes. 2 2019.
- [60] Randy S. Conklin and Bob Holdom. Gravitational wave echo spectra. *Phys. Rev. D*, 100(12):124030, 2019.
- [61] Luis Felipe Longo Micchi, Niayesh Afshordi, and Cecilia Chirenti. How loud are echoes from Exotic Compact Objects? 10 2020.
- [62] T. Damour. The motion of compact bodies and gravitational radiation. In *General Relativity and Gravitation Conference*, pages 89–106, January 1984.
- [63] Éanna É. Flanagan and Tanja Hinderer. Constraining neutron-star tidal love numbers with gravitational-wave detectors. *Physical Review D*, 77(2), Jan 2008.
- [64] Leslie Wade, Jolien D.E. Creighton, Evan Ochsner, Benjamin D. Lackey, Benjamin F. Farr, Tyson B. Littenberg, and Vivien Raymond. Systematic and statistical errors in a bayesian approach to the estimation of the neutron-star equation of state using advanced gravitational wave detectors. *Phys. Rev. D*, 89(10):103012, 2014.
- [65] Feryal Özel and Paulo Freire. Masses, radii, and the equation of state of neutron stars. *Annual Review of Astronomy and Astrophysics*, 54(1):401–440, Sep 2016.
- [66] R. Friedberg, T.D. Lee, and Y. Pang. Scalar Soliton Stars and Black Holes. *Phys. Rev. D*, 35:3658, 1987.
- [67] Michael Kesden, Jonathan Gair, and Marc Kamionkowski. Gravitational-wave signature of an inspiral into a supermassive horizonless object. *Phys. Rev. D*, 71:044015, 2005.
- [68] Thibault Damour and Alessandro Nagar. Relativistic tidal properties of neutron stars. *Phys. Rev. D*, 80:084035, 2009.
- [69] Taylor Binnington and Eric Poisson. Relativistic theory of tidal love numbers. *Physical Review D*, 80(8), Oct 2009.
- [70] Tanja Hinderer. Tidal love numbers of neutron stars. *The Astrophysical Journal*, 677(2):1216–1220, Apr 2008.
- [71] Vitor Cardoso, Luís C. B. Crispino, Caio F. B. Macedo, Hirotada Okawa, and Paolo Pani. Light rings as observational evidence for event horizons: long-lived modes, ergoregions and nonlinear instabilities of ultracompact objects. *Phys. Rev. D*, 90(4):044069, 2014.
- [72] Masaru Shibata and Kōji Uryū. Simulation of merging binary neutron stars in full general relativity: $\gamma = 2$ case. *Physical Review D*, 61(6), Feb 2000.
- [73] Thomas W. Baumgarte, Stuart L. Shapiro, and Masaru Shibata. On the maximum mass of differentially rotating neutron stars. *Astrophys. J.*, 528:L29, 2000.
- [74] Sebastiano Bernuzzi. Neutron Stars Merger Remnants. 4 2020.
- [75] C. Palenzuela, I. Olabarrieta, L. Lehner, and Steven L. Liebling. Head-on collisions of boson stars. *Phys. Rev. D*, 75:064005, 2007.
- [76] Luis Lehner and Frans Pretorius. Numerical Relativity and Astrophysics. *Ann. Rev. Astron. Astrophys.*, 52:661–694, 2014.
- [77] Jocelyn S. Read, Benjamin D. Lackey, Benjamin J. Owen, and John L. Friedman. Constraints on a phenomenologically parameterized neutron-star equation of state. *Phys. Rev. D*, 79:124032, 2009.
- [78] S. Typel, G. Ropke, T. Klähn, D. Blaschke, and H.H. Wolter. Composition and thermodynamics of nuclear matter with light clusters. *Phys. Rev. C*, 81:015803, 2010.
- [79] Tim Dietrich, David Radice, Sebastiano Bernuzzi, Francesco Zappa, Albino Perego, Bernd Brügmann, Swami Vivekanandji Chaurasia, Reetika Dudi, Wolfgang Tichy, and Maximiliano Ujevic. CoRe database of binary neutron star merger waveforms. *Class. Quant. Grav.*, 35(24):24LT01, 2018.
- [80] N. Sanchis-Gual, F. Di Giovanni, M. Zilhão, C. Herdeiro, P. Cerdá-Durán, J. A. Font, and E. Radu. Non-linear dynamics of spinning bosonic stars: formation and stability. *Phys. Rev. Lett.*, 123(22):221101, 2019.
- [81] Fabrizio Di Giovanni, Nicolas Sanchis-Gual, Pablo Cerdá-Durán, Miguel Zilhão, Carlos Herdeiro, José A. Font, and Eugen Radu. On the dynamical bar-mode instability in spinning bosonic stars. 10 2020.
- [82] A. Bauswein, H.-T. Janka, K. Hebeler, and A. Schwenk. Equation-of-state dependence of the gravitational-wave signal from the ring-down phase of neutron-star mergers. *Physical Review D*, 86(6), Sep 2012.
- [83] A. Bauswein and H.-T. Janka. Measuring neutron-star properties via gravitational waves from neutron-star mergers. *Physical Review Letters*, 108(1), Jan 2012.
- [84] A. Bauswein and N. Stergioulas. Unified picture of the post-merger dynamics and gravitational wave emission in neutron star mergers. *Phys. Rev. D*, 91(12):124056, 2015.
- [85] Luis Lehner, Steven L Liebling, Carlos Palenzuela, O L Caballero, Evan O’Connor, Matthew Anderson, and David Neilsen. Unequal mass binary neutron star mergers and multimessenger signals. *Classical and Quantum Gravity*, 33(18):184002, Sep 2016.
- [86] Kentaro Takami, Luciano Rezzolla, and Luca Baiotti. Spectral properties of the post-merger gravitational-wave signal from binary neutron stars. *Phys. Rev.*, D91(6):064001, 2015.
- [87] Matteo Lucca, Laura Sagunski, Federico Guercilena, and Christian M. Fromm. Shedding light on the angular momentum evolution of binary neutron star merger remnants: a semi-analytic model. *JHEAp*, 29:19–30, 2021.
- [88] K. S. Thorne. *Magic without Magic: John Archibald Wheeler*. Oxford science publications. 1972.
- [89] Alejandro Bohé, Lijing Shao, Andrea Taracchini, Alessandra Buonanno, Stanislav Babak, Ian W. Harry, Ian Hinder, Serguei Ossokine, Michael Pürrer, Vivien Raymond, and et al. Improved effective-one-body model of spinning, nonprecessing binary black holes for the era of gravitational-wave astrophysics with advanced detectors. *Physical Review D*, 95(4), Feb 2017.
- [90] LIGO Scientific Collaboration. LIGO Algorithm Library - LALSuite. free software (GPL), 2018.
- [91] Alejandro Bohé et al. Improved effective-one-body model of spinning, nonprecessing binary black holes for the era of gravitational-wave astrophysics with advanced detectors. *Phys. Rev.*, D95(4):044028, 2017.
- [92] Thibault Damour and Alessandro Nagar. A new analytic representation of the ringdown waveform of coalescing spinning black hole binaries. *Phys. Rev.*, D90(2):024054, 2014.
- [93] Emanuele Berti, Vitor Cardoso, and Andrei O. Starinets. Quasinormal modes of black holes and black branes. *Class. Quant. Grav.*, 26:163001, 2009.
- [94] Sascha Husa, Sebastian Khan, Mark Hannam, Michael Pürrer, Frank Ohme, Xisco Jiménez Forteza, and Alejandro Bohé. Frequency-domain gravitational waves from nonprecessing black-hole binaries. I. New numerical waveforms and anatomy of the signal. *Phys. Rev.*, D93(4):044006, 2016.
- [95] Sebastian Khan, Sascha Husa, Mark Hannam, Frank Ohme, Michael Pürrer, Xisco Jiménez Forteza, and Alejandro Bohé. Frequency-domain gravitational waves from nonprecessing

- black-hole binaries. II. A phenomenological model for the advanced detector era. *Phys. Rev.*, D93(4):044007, 2016.
- [96] Pau Amaro-Seoane et al. Laser Interferometer Space Antenna. 2 2017.
- [97] N. Aghanim et al. Planck 2018 results. VI. Cosmological parameters. 2018.
- [98] Curt Cutler and Éanna E. Flanagan. Gravitational waves from merging compact binaries: How accurately can one extract the binary’s parameters from the inspiral waveform? *Physical Review D*, 49(6):2658–2697, Mar 1994.
- [99] B.P. Abbott, R. Abbott, T.D. Abbott, F. Acernese, K. Ackley, C. Adams, T. Adams, P. Addesso, R.X. Adhikari, V.B. Adya, and et al. Gw170817: Observation of gravitational waves from a binary neutron star inspiral. *Physical Review Letters*, 119(16), Oct 2017.
- [100] S Hild, M Abernathy, F Acernese, P Amaro-Seoane, N Andersson, K Arun, F Barone, B Barr, M Barsuglia, M Beker, and et al. Sensitivity studies for third-generation gravitational wave observatories. *Classical and Quantum Gravity*, 28(9):094013, Apr 2011.
- [101] M. Punturo et al. The Einstein Telescope: A third-generation gravitational wave observatory. *Class. Quant. Grav.*, 27:194002, 2010.
- [102] Stefan Ballmer and Vuk Mandic. New Technologies in Gravitational-Wave Detection. *Ann. Rev. Nucl. Part. Sci.*, 65:555–577, 2015.
- [103] Curt Cutler. Angular resolution of the LISA gravitational wave detector. *Phys. Rev. D*, 57:7089–7102, 1998.
- [104] Travis Robson, Neil J. Cornish, and Chang Liu. The construction and use of LISA sensitivity curves. *Class. Quant. Grav.*, 36(10):105011, 2019.
- [105] Ka Wa Tsang, Tim Dietrich, and Chris Van Den Broeck. Modeling the postmerger gravitational wave signal and extracting binary properties from future binary neutron star detections. *Phys. Rev. D*, 100(4):044047, 2019.
- [106] Katerina Chatziioannou, James Alexander Clark, Andreas Bauswein, Margaret Millhouse, Tyson B. Littenberg, and Neil Cornish. Inferring the post-merger gravitational wave emission from binary neutron star coalescences. *Phys. Rev. D*, 96(12):124035, 2017.
- [107] Matteo Breschi, Sebastiano Bernuzzi, Francesco Zappa, Michalis Agathos, Albino Perego, David Radice, and Alessandro Nagar. kiloHertz gravitational waves from binary neutron star remnants: time-domain model and constraints on extreme matter. *Phys. Rev. D*, 100(10):104029, 2019.
- [108] B. P. Abbott et al. GWTC-1: A Gravitational-Wave Transient Catalog of Compact Binary Mergers Observed by LIGO and Virgo during the First and Second Observing Runs. 2018.
- [109] T.A. Apostolatos. Search templates for gravitational waves from precessing, inspiraling binaries. *Phys. Rev. D*, 52:605–620, 1995.
- [110] Thibault Damour, Bala R. Iyer, and B.S. Sathyaprakash. Improved filters for gravitational waves from inspiralling compact binaries. *Phys. Rev. D*, 57:885–907, 1998.
- [111] J. Abadie et al. Search for Gravitational Waves from Low Mass Compact Binary Coalescence in LIGO’s Sixth Science Run and Virgo’s Science Runs 2 and 3. *Phys. Rev. D*, 85:082002, 2012.
- [112] J. Aasi et al. Search for gravitational waves from binary black hole inspiral, merger, and ringdown in LIGO-Virgo data from 2009–2010. *Phys. Rev. D*, 87(2):022002, 2013.
- [113] Bruce Allen, Warren G. Anderson, Patrick R. Brady, Duncan A. Brown, and Jolien D.E. Creighton. FINDCHIRP: An Algorithm for detection of gravitational waves from inspiraling compact binaries. *Phys. Rev. D*, 85:122006, 2012.
- [114] F. Feroz, M. P. Hobson, and M. Bridges. MultiNest: an efficient and robust Bayesian inference tool for cosmology and particle physics. *Mon. Not. Roy. Astron. Soc.*, 398:1601–1614, 2009.
- [115] Alberto Sesana, Francesco Haardt, Piero Madau, and Marta Volonteri. Low - frequency gravitational radiation from coalescing massive black hole binaries in hierarchical cosmologies. *Astrophys. J.*, 611:623–632, 2004.
- [116] A. Sesana, F. Haardt, P. Madau, and M. Volonteri. The gravitational wave signal from massive black hole binaries and its contribution to the LISA data stream. *Astrophys. J.*, 623:23–30, 2005.
- [117] Antoine Klein et al. Science with the space-based interferometer eLISA: Supermassive black hole binaries. *Phys. Rev. D*, 93(2):024003, 2016.
- [118] Matteo Bonetti, Alberto Sesana, Francesco Haardt, Enrico Barausse, and Monica Colpi. Post-Newtonian evolution of massive black hole triplets in galactic nuclei – IV. Implications for LISA. *Mon. Not. Roy. Astron. Soc.*, 486(3):4044–4060, 2019.
- [119] Michael L. Katz, Luke Zoltan Kelley, Fani Dosopoulou, Samantha Berry, Laura Blecha, and Shane L. Larson. Probing Massive Black Hole Binary Populations with LISA. *Mon. Not. Roy. Astron. Soc.*, 491(2):2301–2317, 2020.
- [120] P. Dayal, E. M. Rossi, B. Shiralilou, O. Piana, T. R. Choudhury, and M. Volonteri. The hierarchical assembly of galaxies and black holes in the first billion years: predictions for the era of gravitational wave astronomy. *Mon. Not. Roy. Astron. Soc.*, 486:2336–2350, June 2019.
- [121] Enrico Barausse, Irina Dvorkin, Michael Tremmel, Marta Volonteri, and Matteo Bonetti. Massive black hole merger rates: the effect of kpc separation wandering and supernova feedback. 6 2020.
- [122] R. Abbott et al. GWTC-2: Compact Binary Coalescences Observed by LIGO and Virgo During the First Half of the Third Observing Run. 10 2020.
- [123] Juan Calderón Bustillo, Nicolas Sanchis-Gual, Alejandro Torres-Forné, José A. Font, Avi Vajpeyi, Rory Smith, Carlos Herdeiro, Eugen Radu, and Samson H.W. Leong. The (ultra) light in the dark: A potential vector boson of 8.7×10^{-13} eV from GW190521. 9 2020.